The Astrophysical Journal, 928:66 (16pp), 2022 March 20 https://doi.org/10.3847/1538-4357/ac54af
© 2022. The Author(s). Published by the American Astronomical Society.
OPEN ACCESS

In Situ Measurement of the Energy Fraction in Suprathermal and Energetic Particles at ACE, Wind, and PSP Interplanetary Shocks

Liam David[1], Federico Fraschetti[1,2], Joe Giacalone[1], Robert F. Wimmer-Schweingruber[3,4], Lars Berger[3], and David Lario[5]
[1] Lunar & Planetary Laboratory, University of Arizona, Tucson, AZ 85721, USA
[2] Center for Astrophysics | Harvard & Smithsonian, Cambridge, MA, 02138, USA
[3] Institute of Experimental and Applied Physics, Kiel University, Kiel, Germany
[4] National Space Science Center, Chinese Academy of Sciences, Beijing, People's Republic of China
[5] Heliophysics Science Division, NASA Goddard Space Flight Center, Greenbelt, MD 20771, USA
Received 2021 December 7; revised 2022 January 26; accepted 2022 February 12; published 2022 March 28

Abstract

The acceleration of charged particles by interplanetary shocks (IPs) can drain a nonnegligible fraction of the plasma pressure. In this study, we have selected 17 IPs observed in situ at 1 au by the Advanced Composition Explorer and the Wind spacecraft, and 1 shock at 0.8 au observed by Parker Solar Probe. We have calculated the time-dependent partial pressure of suprathermal and energetic particles (smaller and greater than 50 keV for protons and 30 keV for electrons, respectively) in both the upstream and downstream regions. The particle fluxes were averaged for 1 hr before and 1 hr after the shock time to remove short timescale effects. Using the MHD Rankine–Hugoniot jump conditions, we find that the fraction of the total upstream energy flux transferred to suprathermal and energetic downstream particles is typically $\lesssim$16%, in agreement with previous observations and simulations. Notably, by accounting for errors on all measured shock parameters, we have found that for any given fast magnetosonic Mach number, $M_f < 7$, the angle between the shock normal and average upstream magnetic field, θ_{Bn}, is not correlated with the energetic particle pressure; in particular, the partial pressure of energized particles does not decrease for $\theta_{Bn} \gtrsim 45°$. The downstream electron-to-proton energy ratio in the range $\gtrsim$ 140 eV for electrons and $\gtrsim$ 70 keV for protons exceeds the expected ∼1% and nears equipartition (>0.1) for the Wind events.

Unified Astronomy Thesaurus concepts: Interplanetary shocks (829); Interplanetary particle acceleration (826); Space plasmas (1544)

1. Introduction

Shock waves are ubiquitous in space and astrophysical plasmas (Treumann 2009). A shock converts incoming kinetic energy into downstream thermal and magnetic energy with a certain, usually small, fraction in energized charged particles (e.g., Drury 1983). In the late 1970s (e.g., Gosling et al. 1981), evidence of direct extraction of accelerated particles from the thermal populations was provided by combining International Sun-Earth Explorers-2 (ISEE-2) and ISEE-3 observations. However, only a handful of studies have investigated in situ measurements of the energy fraction in the energized particles. The contribution of suprathermal and energetic ions ($\gtrsim$10 keV) and electrons ($\gtrsim$100 eV) to the energy balance at interplanetary shocks (IPs) has been quantified only indirectly and in only a few instances. Mewaldt et al. (2008) estimated that in large coronal mass ejections (CMEs; inferred kinetic energy $> 10^{31}$ erg), the fraction of the bulk kinetic energy transferred into particles presumably accelerated by the shocks driving the CMEs can attain 10%–20%. Likewise, from a comparative estimate of the energy fractions in the magnetic field, the flare-associated energetic particles, and the CME bulk motion of 38 large solar events, Emslie et al. (2012) concluded that between 0.4% and 20% of the CME kinetic energy in the solar wind frame is stored in solar energetic particles accelerated by the associated IPs. From a multispacecraft study of 10 solar energetic particle events, a comparable fraction was obtained (Aschwanden et al. 2017), under the assumption that particles are accelerated at CME-driven shocks. In some cases, the transfer of a significant fraction of the upstream ram pressure into energized charged particles causes their partial pressure (i.e., the kinetic pressure of the suprathermal and energetic particles combined) to equal or exceed the magnetic field pressure, an effect observed by Lario & Decker (2002), Marhavilas & Sarris (2011), Russell et al. (2013), and Lario et al. (2015). However, to our knowledge, in situ measurements of the energy content in energized particles at shocks are lacking.

The observations described above suggest that the effect of energized particles on the energy balance at shocks cannot be ignored and that the modeling of shock secular evolution must account for it. In addition, observational studies of the energized electron-to-ion energy ratio have not been extensively pursued. IPs are unique among shocks since the energy fraction in energized particles can be measured accurately and directly; for extra-solar shocks, the energy partition can only be inferred indirectly and relies on models of the radiation emission mechanism.

An analysis of 258 Wind IPs (Reames 2012) found that a high θ_{Bn}, along with a high shock speed and compression ratio, is correlated with events showing large particle acceleration signatures in 1–10 MeV/nucl He ions. This result is consistent with the long-known result that shocks with $\theta_{Bn} > 45°$ are rapid accelerators (Jokipii 1982, 1987). The acceleration efficiency at

Original content from this work may be used under the terms of the Creative Commons Attribution 4.0 licence. Any further distribution of this work must maintain attribution to the author(s) and the title of the work, journal citation and DOI.

quasi-perpendicular shocks can exceed that at quasi-parallel shocks, provided there is sufficient preexisting large-scale magnetic turbulence present in the upstream region (Giacalone 2005a, 2005b; Fraschetti & Giacalone 2015). However, the error estimate on the shock parameters plays a pivotal role in any robust conclusion on the efficiency of particle acceleration at the shock.

Combining observations from the Advanced Composition Explorer (ACE) and the Wind spacecraft for a number of IPs, Lario et al. (2019) showed that the upstream energy spectrum starts deviating from thermal and exhibits a significant suprathermal energized ion component within only a few minutes of the shock. This result suggests that the particle partial pressure can rapidly vary as the shock approaches the spacecraft. Thus, the time evolution of the particle pressure needs to be monitored beginning several hours before the shock to identify its role in the acceleration process.

Early-on hybrid simulations (kinetic ions/fluid electrons) also found that the downstream energetic ion partial pressure flux is at most 10%–25% of the upstream ram energy flux (Giacalone et al. 1997). Moreover, such a fraction was found to be roughly independent of the magnetic obliquity for the quasi-parallel shocks analyzed ($\theta_{\rm Bn} \leqslant 30°$, as larger values of $\theta_{\rm Bn}$ were not considered therein) and also independent of Alfvén Mach numbers $\geqslant$6 for a fixed sonic Mach number (Giacalone et al. 1997). Monte Carlo simulations modeling particle acceleration at the terrestrial bow shock (Ellison & Moebius 1987) measured by the Active Magnetospheric Particle Tracer Explorers/Ion Release Module found that particles with energy per charge $>$10 keV/Q drain on the order of a few percent of the upstream ram energy flux. A comparison of Monte Carlo and 1D hybrid simulations (Ellison et al. 1993) yielded close agreement for proton and heavy ion distribution functions between both approaches, concluding that the minimum energy fraction in $>$10 keV protons is $\sim$10%.

Comparable energy fractions seem to be drained into energized particles at other types of shocks. Upon crossing the solar wind termination shock, Voyager 2 measured the temperature of the shock-heated plasma to be roughly 10 times smaller than expected from the MHD jump conditions since a large fraction of the solar wind energy is likely transferred to the pick-up ions (Richardson et al. 2008). The partial pressure of ions $>$ 28 keV was measured to be comparable to, or exceed, that of the thermal ion population, and was about twice as large as the magnetic field pressure (Decker et al. 2008). At Earth's bow shock, at least 15% and as much as 20% of the incident solar wind energy flux is converted into energetic particles above $\sim$10 keV/Q (Ellison et al. 1990). Slane et al. (2014) inferred that a nonnegligible fraction of the bulk kinetic energy (16%) is converted into accelerated particles in the Tycho's supernova remnant (SNR) shock by using a hydrodynamic model of the broadband spectrum (from radio to multi-TeV radiation). A comparable fraction of accelerated protons to the total initial kinetic energy was found for the two extragalactic supernova remnants N132D (Bamba et al. 2018) and 0509-67.5 (Hovey et al. 2015).

In this paper, we consider a number of IPs at 1 au with accurately determined shock parameters; such a selection allows unambiguous conclusions to be drawn for the first time on the efficiency on the particle energization (from suprathermal up to hundreds of MeV) over a broad range of magnetic obliquity and Mach number. In particular, we combine, for a sample of 17 IPs, data sets for the thermal plasma momenta and for the suprathermal/high-energy tail of the proton and electron energy spectra to determine the fraction of the shock energy density that is transferred into the non-Maxwellian particle populations for a broad range of $\theta_{\rm Bn}$ and the fast magnetosonic Mach number M_f. The distinction between suprathermal ($\lesssim$50 keV for protons, and $\lesssim$30 keV for electrons) and energetic ($\gtrsim$50 keV for protons, and $\gtrsim$30 keV for electrons) particles is herein made according to the nominal energy ranges of the instruments used in this analysis. Since a single integral of energy spectrum is calculated for each particle population over the entire available energy range, the distinction between suprathermal and energetic particles has no physical effect. We find that, for any given interval of M_f, the relative energy spent in energizing particles does not decrease with $\theta_{\rm Bn}$ and increases with M_f. We also include one of the first IPs observed in situ by Parker Solar Probe (PSP) at 0.8 au.

Section 2 details our data sources, gives an overview of the detectors on ACE and Wind used in this work, outlines our shock selection criteria, and describes all data pre-processing steps. In Section 3 we describe our analysis methods, including coordinate transformations, determination of energized particle properties, and error propagation. Section 4 outlines our results. We characterize the overall energy conservation, the fluxes of energized protons and electrons, and the trends within a 6 hr time window of each shock. Section 5 discusses known sources of error and broader implications of this study. Section 6 summarizes the main conclusions of this work and discusses avenues for future research.

2. Data Sampling

2.1. Data Sources

The Center for Astrophysics | Harvard & Smithsonian (CfA) shocks database, used in the present study, catalogs IPs observed by the ACE and Wind spacecraft, providing shock parameters including the time, speed, and shock normal direction, as well as plasma parameters such as proton temperatures, proton densities, and magnetic fields both upstream and downstream of the shock using the RH08 method (Szabo 1994; Koval & Szabo 2008). The RH08 method determines the shock speed and the shock normal direction independently using a multiparameter optimization approach, thereby demonstrating the uniqueness of the solution. For dynamically varying quantities such as the magnetic field, the database uses adaptive averaging within roughly $\pm$20 minutes of the shock time both upstream and downstream.

2.2. Shock Selection

We selected eight fast-forward shocks observed in situ by ACE and nine by Wind between 1997 and 2013, which are listed in Tables 1 and 2. These tables include all asymptotic ($\sim$20 minutes before and after the shock passage) plasma parameters relevant to our analysis. In particular, we provide M_f, the shock speed in the spacecraft frame $V_{\rm sh}$, $\boldsymbol{V}_{\rm up} \cdot \hat{\boldsymbol{n}}$, and $\boldsymbol{V}_{\rm down} \cdot \hat{\boldsymbol{n}}$ in the spacecraft reference frame (where $\boldsymbol{n}$ is the unit vector normal to the shock surface and $\boldsymbol{V}_{\rm up}$ and $\boldsymbol{V}_{\rm down}$ are the upstream and downstream flow velocities, respectively), the thermal proton densities $n_{\rm up}$ and $n_{\rm down}$, and temperatures $T_{\rm up}$ and $T_{\rm down}$, $\theta_{\rm Bn}$, and the magnetic energy densities $\boldsymbol{B}_{\rm up}^2/8\pi$ and $\boldsymbol{B}_{\rm down}^2/8\pi$. Since errors on the shock speed and normal

Table 1
Selected Wind and ACE Shock Parameters Relevant to Our Analysis, Retrieved from the CfA (cfa.harvard.edu/shocks) Database

Shock (Spacecraft Year/Day/UT) [doy]	M_f	$V_{\rm sh}$ (km s^{-1})	$\boldsymbol{V}_{\rm up}^{(sc)} \cdot \hat{\boldsymbol{n}}$ (km s^{-1})	$\boldsymbol{V}_{\rm down}^{(sc)} \cdot \hat{\boldsymbol{n}}$ (km s^{-1})	$n_{\rm up}$ (cm^{-3})	$n_{\rm down}$ (cm^{-3})	$T_{\rm up}$ (10^4 K)	$T_{\rm down}$ (10^4 K)	$\theta_{\rm Bn}$ (degrees)
A 2001/298/8:2:1 [298.3347]	5.7 ± 0.7	477.7 ± 8.7	327.4 ± 3.4	438.0 ± 16.1	4.9 ± 0.6	18.5 ± 1.4	0.6 ± 0.2	7.6 ± 2.3	40.0 ± 7.9
A 2005/21/16:47:26 [21.6996]	5.3 ± 0.6	1076.6 ± 8.7	598.2 ± 23.6	899.3 ± 16.5	5.9 ± 0.6	15.9 ± 3.1	10.6 ± 1.2	39.4 ± 8.9	69.8 ± 17.8
A 1999/49/2:8:50 [49.0895]	3.6 ± 0.2	718.5 ± 3.7	398.7 ± 7.0	596.7 ± 10.0	3.9 ± 0.6	10.6 ± 1.0	6.5 ± 0.6	31.8 ± 3.4	50.8 ± 7.4
A 1999/346/15:14:36 [346.6352]	1.7 ± 0.1	521.9 ± 3.7	323.1 ± 15.3	432.5 ± 20.3	0.8 ± 0.1	1.8 ± 0.3	2.2 ± 0.5	17.2 ± 3.7	68.3 ± 10.0
A 2001/23/10:6:20 [23.4211]	2.9 ± 0.4	582.4 ± 16.6	415.0 ± 4.9	546.5 ± 12.0	2.7 ± 0.4	13.0 ± 0.6	5.0 ± 0.9	30.6 ± 2.0	19.2 ± 8.3
A 2001/86/17:15:15 [86.7189]	1.5 ± 0.2	566.3 ± 17.4	394.1 ± 5.9	486.3 ± 12.4	7.4 ± 0.6	16.0 ± 1.0	11.3 ± 0.7	19.0 ± 0.8	74.4 ± 3.6
A 2001/118/4:31:58 [118.1889]	4.5 ± 0.7	906.4 ± 57.8	456.6 ± 8.2	752.3 ± 10.4	3.5 ± 0.4	11.0 ± 2.5	3.1 ± 0.7	30.8 ± 4.3	89.7 ± 4.1
A 2001/229/10:16:2 [229.4278]	2.8 ± 0.3	503.8 ± 8.9	343.9 ± 4.5	469.9 ± 5.5	3.8 ± 0.5	17.9 ± 1.2	1.5 ± 0.2	5.3 ± 0.5	79.8 ± 5.0
W 2003/308/6:46:4 [308.2820]	2.7 ± 0.4	762.3 ± 18.3	480.1 ± 7.4	722.6 ± 14.5	2.6 ± 0.6	19.1 ± 1.9	18.8 ± 6.6	104.8 ± 11.3	63.9 ± 11.7
W 1997/326/9:12:52 [326.3839]	2.3 ± 0.1	489.6 ± 7.9	344.6 ± 1.9	432.9 ± 6.6	11.7 ± 0.5	29.0 ± 0.2	6.8 ± 0.4	24.1 ± 3.4	83.3 ± 3.6
W 2013/275/1:15:49 [275.0527]	4.2 ± 0.2	654.3 ± 1.5	371.1 ± 4.6	563.4 ± 9.3	6.5 ± 0.3	20.0 ± 1.4	8.6 ± 1.0	68.5 ± 21.2	28.6 ± 8.3
W 2004/312/17:59:5 [312.7494]	2.1 ± 0.2	751.2 ± 27.9	437.8 ± 9.0	611.2 ± 15.0	18.1 ± 0.8	41.0 ± 5.4	36.4 ± 3.5	65.3 ± 7.2	60.9 ± 3.4
W 1998/275/7:6:4 [275.2959]	2.6 ± 0.9	620.3 ± 77.0	349.7 ± 14.7	519.2 ± 20.8	2.8 ± 1.1	7.7 ± 1.1	11.0 ± 5.0	44.2 ± 13.2	26.2 ± 9.9
W 2013/76/5:21:28 [76.2232]	5.9 ± 0.4	766.6 ± 9.8	425.1 ± 2.9	639.6 ± 23.3	3.3 ± 0.2	9.4 ± 2.1	4.8 ± 0.8	49.8 ± 26.2	35.1 ± 5.8
W 2002/77/13:14:4 [77.5514]	5.7 ± 0.9	580.0 ± 39.7	310.9 ± 8.1	470.8 ± 7.1	15.5 ± 2.4	37.4 ± 3.4	4.2 ± 0.7	16.3 ± 4.1	44.2 ± 20.3
W 2004/208/22:25:23 [208.9343]	5.5 ± 0.7	1105.7 ± 50.5	593.5 ± 5.8	966.1 ± 24.0	2.0 ± 0.2	7.2 ± 1.1	13.3 ± 1.8	123.1 ± 25.2	57.8 ± 7.0
W 2005/252/13:33:1 [252.5646]	6.3 ± 0.5	620.3 ± 9.0	315.1 ± 2.9	478.1 ± 11.3	13.7 ± 1.3	30.1 ± 4.7	3.2 ± 0.2	17.3 ± 4.3	89.8 ± 8.6

Note. Since the temperatures were not provided in the CfA database, they were calculated from the provided thermal speed W_i using $\frac{3}{2}k_BT = \frac{1}{2}m_pW_i^2$. See Table 2 for magnetic field values.

Table 2
Asymptotic Magnetic Field Energy Densities Retrieved from the CfA (cfa.harvard.edu/shocks) Database

Shock (Spacecraft Year/Day/UT) [doy]	$\frac{B_{up}^2}{8\pi}$ (10^{-10}erg cm^{-3})	$\frac{B_{up}^2}{8\pi}$ (10^{-10}erg cm^{-3})
A 2001/298/8:2:1 [298.3347]	0.2 ± 0.0	2.1 ± 0.7
A 2005/21/16:47:26 [21.6996]	1.5 ± 0.8	12.3 ± 7.6
A 1999/49/2:8:50 [49.0895]	2.1 ± 0.4	12.9 ± 1.7
A 1999/346/15:14:36 [346.6352]	0.9 ± 0.2	4.1 ± 0.4
A 2001/23/10:6:20 [23.4211]	0.6 ± 0.1	1.2 ± 0.6
A 2001/86/17:15:15 [86.7189]	5.4 ± 0.5	21.1 ± 2.3
A 2001/118/4:31:58 [118.1889]	2.5 ± 0.5	22.5 ± 3.6
A 2001/229/10:16:2 [229.4278]	0.8 ± 0.1	13.6 ± 3.3
W 2003/308/6:46:4 [308.2820]	0.5 ± 0.5	4.1 ± 5.7
W 1997/326/9:12:52 [326.3839]	1.2 ± 0.2	5.5 ± 2.4
W 2013/275/1:15:49 [275.0527]	1.2 ± 0.3	3.5 ± 1.5
W 2004/312/17:59:5 [312.7494]	14.3 ± 1.7	75.9 ± 4.9
W 1998/275/7:6:4 [275.2959]	1.7 ± 0.4	10.4 ± 2.7
W 2013/76/5:21:28 [76.2232]	0.6 ± 0.1	1.9 ± 2.5
W 2002/77/13:14:4 [77.5514]	0.9 ± 0.5	9.6 ± 6.7
W 2004/208/22:25:23 [208.9343]	0.6 ± 0.1	10.0 ± 4.5
W 2005/252/13:33:1 [252.5646]	1.2 ± 0.3	5.4 ± 2.0

direction have the greatest effect on our final uncertainties, these were our most limiting selection criteria. A compression ratio greater than two was required, as was a fast magnetosonic Mach number $M_f \gtrsim 1.5$. We chose M_f rather than the Alfvén Mach number M_A since the former depends on both the sound speed and Alfvén speed, thus better capturing the characteristics of the background plasma environment. In order to examine the relation between M_f and θ_{Bn}, we selected shocks with a range of values: the Mach numbers ranged from 1.49 to 6.21, characteristic of IPs, and θ_{Bn} spanned from 19.2° to 89.8° (see Table 1). Only a small fraction of the intensity profiles of energized protons show a discernible quasi-exponential preshock rise, with small-amplitude fluctuations, followed by a flat top in the downstream plasma region, as predicted in the linear diffusive shock acceleration (DSA) scenario (Parker 1965). In order to minimize the error estimates in the energy fluxes, we thoroughly scanned the spacecraft archives; several shocks were included with particle intensity profiles deviating from the DSA prediction (see Lario et al. 2003 for a shock classification scheme of the ACE archive for years 1999–2003 based on ~47 keV ion and ~38 keV electron intensity-time profiles).

PSP was crossed by a CME-driven IPs on 2020 November 30, at a distance of 0.81 au from the Sun, and recorded one of the highest energetic particle intensities observed thus far in this mission (Mitchell et al. 2021; Giacalone et al. 2021; Lario et al. 2021). The shock occurred at a time when PSP was near its farthest point from the Sun in its seventh orbit and close to 1 au like the other measurements presented in our study; thus, it has been included in this analysis. However, due to the poor quality of data available for this event, we excluded it from our final shock statistics. Special steps that differ from the ACE/Wind shocks are discussed below.

2.3. Energized Particle Fluxes

2.3.1. ACE Particle Data

Proton data for the ACE shocks were retrieved from the Electron, Proton, and Alpha Monitor (EPAM) through the CalTech Level 2 Database;[6] the Solar Wind Ion Composition Spectrometer (SWICS) instrument data were also gathered. EPAM contains a Low Energy Magnetic Spectrometer, designated LEMS120, that points 120° off the spacecraft spin axis, where the ACE spin axis points mostly toward the Sun within ±20°. It records ion intensities between 47.0 keV and 4.80 MeV in eight energy bins during the 12 s of the spacecraft spin period (Gold et al. 1998). This energy range, and those of all instruments described below, are displayed in Figure 1, and fluxes were converted into units of cm^{-2}s^{-1}sr^{-1}eV^{-1}. SWICS is a linear time-of-flight mass spectrometer with electrostatic deflection, allowing it to measure ion mass, charge, and energy. A full energy spectrum covering 657 eV − 86.6 keV in 58 bins is collected every 12 minutes; each bin is integrated serially for 12 s (Gloeckler et al. 1998). SWICS can disentangle the background thermal solar wind, suprathermal protons, and heavier ions, and here we consider only proton observations. Since EPAM extends down to 47.0 keV and has both a higher time resolution and smaller errors than SWICS, we removed the highest four SWICS energy bins, consisting of protons above 48.8 keV, to eliminate overlap. In the overlapping energy region, SWICS intensities computed assuming isotropic fluxes may exhibit a lower value (by a factor of ~2) than the EPAM intensities averaged over the same time interval, implying a possible discrepancy among instrument calibrations.

The formulation of DSA applies only to sufficiently isotropic (i.e., sufficiently fast) particles in the local plasma frame Parker (1965) that can be efficiently accelerated by undergoing frequent pitch-angle scattering. Hybrid simulations (e.g., Giacalone et al. 1997) suggest a reasonable cutoff of 10 times the plasma ram energy, namely $v \gtrsim 3V_{sh}$, where v is particle speed in the spacecraft frame and V_{sh} is also measured in the spacecraft frame. Thus, SWICS data below the DSA cutoff were not included (see Figure 1).

Spin-averaged electron data for the ACE shocks were obtained from the Deflected Electrons (DE30) instrument, which points 30° off the spin axis, through the NASA CDAWeb database.[7] Four energy bins span 38 keV–315 keV, and the time resolution is 12 s. A magnetic deflector separates these electrons from the parent LEMS30 instrument, which are measured, although with an elevated instrumental background, by a totally depleted surface barrier silicon detector (Gold et al. 1998).

2.3.2. Wind Particle Data

Omnidirectional proton flux data for the Wind shocks were obtained from the Three-Dimensional Plasma and Energetic Particle Investigation (3DP) instrument through the NASA CDAWeb database. The pertinent detector is a solid-state telescope with a 36° × 20° field of view 126° off the spin axis, which points perpendicular to the ecliptic plane. Nine ion energy bins span 67.3 keV − 6.76 MeV and are integrated in parallel for 12 s samples.

We also considered proton fluxes in the energy range 400 eV − 19.1 keV from the PESA-Hi (PH) data product; however, only one or two of the highest PH energy bins lie beyond the DSA cutoff. Moreover, variations in the definition of the energy bins, as well as uncertainties in estimating the energy flux, led us to discard the PH energy range. Likewise,

[6] http://www.srl.caltech.edu/ACE/ASC/level2/lvl2DATA_EPAM.html
[7] https://cdaweb.gsfc.nasa.gov/index.html

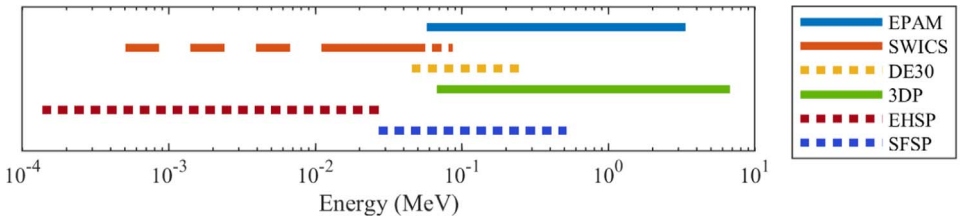

Figure 1. Instrument energy ranges used in this study for both protons (solid) and electrons (dotted). The lowest energies of SWICS are dashed, indicating the range below the DSA cutoff for all shocks. The highest four SWICS energy bins, which were discarded to eliminate overlap with EPAM, are dotted.

we did not include here Wind/SMS/STICS (SupraThermal Ion Composition Spectrometer) data (Gloeckler et al. 1995) that covers the ion energy range 6–230 keV/e, because the reported fluxes[8] for the selected events are vanishing for most of the angular sectors within ±3 hr of each shock.

Wind 3DP also contains two electron data products: EHSP spans 136 eV − 27.6 keV in 15 energy bins, and SFSP covers 27.0 keV − 517 keV in seven bins. Omnidirectional data with a ∼ 24 s resolution were obtained from the NASA CDAWeb database. EHSP data are compiled from the high-range Electron Electrostatic Analyzer (EH), which has a 360° × 90° field of view and works by electrostatic deflection and microchannel plate detection. SFSP data are from the Solid State Foil Telescope (SF) instrument having a 180° × 20° field of view across five apertures. See Lin et al. (1995) for a full description of these instruments. We did not compensate for the small overlap (0.6 keV) between SFSP and EHSP since removing either the highest EHSP or lowest SFSP energy bin would leave a large energy range (18.9 keV–27.0 keV or 27.6 keV–40.1 keV, respectively) unaccounted for.

2.3.3. PSP Particle Data

We obtained energized proton fluxes from the Integrated Science Investigation of the Sun (IS⊙IS), Energetic Particle Instruments (EPI-Lo and EPI-Hi), which measure ion energies in the ranges ∼20 keV/nuc-15 MeV and ∼1–200 MeV/nuc, respectively. EPI-Lo is a TOF mass spectrometer capable of particle species differentiation using a solid-state detector (SSD), and EPI-Hi uses ion-implanted SSDs and the dE/dx versus energy method for both energy and species determination (McComas et al. 2016). For the PSP event that occurred on 2020 November 30, EPI-Hi fluxes are unavailable above 20 MeV and before 2020 December 1 at 4:29:57 UT, corresponding to the first 10 hr after the shock passage. This event is added herein only to compare the order of magnitude of the PSP in situ measurements for a particularly strong event at 0.8 au with those at 1 au. Electrons are not included due to the significant uncertainties in the measurements of this event.

3. Analysis Method

3.1. ACE and Wind Shocks

For the ACE and Wind shocks, the upstream and downstream particle fluxes were found by averaging each energy bin for 1 hr. The interval upstream ended 1 minute before the shock crossing, and the interval downstream began 1 minute after the shock time to best match the CfA database plasma parameters. Ideally the analysis window would have to be reduced to $\lesssim$20 minutes to match the CfA plasma quantities, which are typically averaged over 10–20 minutes within 20 minutes of the shock time. However, this choice would be in conflict with the lower SWICS time resolution (12 minutes), and five samples were deemed necessary to reduce the effects of fluctuations in the data. Therefore, we used 300-sample averages for EPAM, DE30, and 3DP, and 150-sample averages for EHSP and SFSP, to maintain a consistent 1 hr duration across measurements from the different instruments.

We are interested in the contribution of energized particles with speeds $v \gtrsim 3V_{sh}$ to the enthalpy flux (partial pressure times the bulk flow speed). The maximum shock speed V_{sh} in our data set is 1, 105.7 ± 50.5 km/s, so the minimum energy cutoffs across the entire sample in the downstream medium for protons and electrons are 57.4 keV and 31.3 eV, respectively. For the slowest shock ($V_{sh} = 477.7 \pm 8.7$ km/s), these cutoffs are reduced to 10.7 keV and 5.84 eV. SWICS energy bins (minimum energy 657 eV) are below these thresholds and extend into the thermal part of the proton spectrum. As mentioned in Section 2.3.1, for the energized particle contribution, we use only those SWICS fluxes above the energy cutoff, which was calculated individually for each shock. Notably, the nominal lower energies for the remaining low-energy instruments, DE30, 3DP, and SFSP, lie above the DSA cutoff, hence excluding parts of the energized particle populations. The unaccounted for energy ranges involve electrons ∼ 6 eV − 38 keV for ACE, and both protons ∼ 10.7 keV − 67.3 keV and electrons ∼ 6 eV − 138 eV for Wind. Since particle fluxes increase with decreasing energy, the calculated downstream suprathermal Wind proton partial pressures lack a possibly nonnegligible contribution in the range ∼ 10.7 keV − 67.3 keV. See Section 5.2 for further discussion.

A fraction of the bulk incoming kinetic energy is channeled into producing low-energy suprathermal ion populations reflected after single or multiple shock encounters, i.e., field-aligned beam and gyrophase bunched, respectively, whose admixture was studied as a function of distance from the shock in 2D simulations by Savoini et al. (2013). The typical energy of both populations, as measured at IPs, can be as high as ∼ 20 keV (e.g., Kajdič et al. 2017), higher than the ∼ 10 keV measured at the Earth bow shock (e.g., Meziane et al. 2005). Thus, such ion populations overlap only marginally with the energy range here analyzed (protons >10.7 keV–57.4 keV and electrons >5.84 eV–31.3 eV). Therefore, restricting the partial pressure of energized particles to only the downstream medium does not exclude the upstream reflected ion components, relevant only at lower energies. Finally, the partial pressure in the upstream medium requires disentangling the pristine incoming energized particles from the shock-reflected ones.

[8] https://spdf.gsfc.nasa.gov/pub/data/wind/sms/l2/stics/vdf_ascii/solarwind/

The 3D velocity distribution necessary for this task is available only for Wind data and was not considered in this work.

The CfA database parameters, as well as the particle fluxes, are provided in the spacecraft reference frame, whereas the jump conditions are usually, and conveniently, expressed in the shock reference frame. The observed upstream and downstream solar wind velocities were converted to the shock frame using

$$v_{\rm up/down}^{\rm (sh)} = \boldsymbol{V}_{\rm up/down}^{(sc)} - V_{\rm sh}^{(sc)}\hat{\boldsymbol{n}}. \quad (1)$$

Subsequent equations will use identical superscripting where (*sh*) denotes the shock frame and (*sc*) the spacecraft frame.

The particle energies for all instruments were relativistically transformed into the shock frame. We used the energies given by the geometric means of the energy/momentum bins $E_s^{(sc)}$. Subscript s denotes a quantity corresponding to a particle species (protons and electrons). Velocities in the spacecraft frame are defined as

$$v_s^{(sc)} = c\sqrt{1 - \left(\frac{E_p^{(sc)}}{m_s c^2} + 1\right)^{-2}}, \quad (2)$$

where m_s is the rest mass of species s, and then are boosted using

$$v_s^{\rm (sh)} = \frac{v_s^{(sc)} - V_{\rm sh}^{(sc)}}{1 - \frac{v_s^{(sc)} V_{\rm sh}^{(sc)}}{c^2}}. \quad (3)$$

The shock-frame momenta and energies are

$$p_s^{\rm (sh)} = \gamma m_s v_s^{\rm (sh)}, \quad (4)$$

$$E_s^{\rm (sh)} = (\gamma - 1) m_s c^2, \quad (5)$$

where γ is the relativistic gamma factor involving $v_s^{\rm (sh)}$. The fluxes are assumed, both upstream and downstream, to be isotropic, meaning the particle mass density and pressure are

$$\rho_s = 4\pi m_s \int_{p_{\rm min}}^{p_{\rm max}} F dp_s^{\rm (sh)}, \quad (6)$$

$$P_s = \frac{4}{3}\pi m_s \int_{E_{\rm min}}^{E_{\rm max}} \gamma v_s^{\rm (sh)} F dE_s^{\rm (sh)}. \quad (7)$$

Here the flux F is measured in $\rm cm^{-2}\,s^{-1}\,sr^{-1}\,eV^{-1}$. The integrals were approximated using the trapezoidal method.

The gas and particle specific enthalpies were calculated using

$$h_s = \frac{\Gamma}{\Gamma - 1}\frac{P_s}{\rho_s}. \quad (8)$$

Here $\Gamma = 5/3$ is the adiabatic index, which is set by our assumption of a monatomic gas, and P_s and ρ_s are the pressures and mass densities. The magnetic field was not transformed into the shock frame since the shocks are nonrelativistic.

The Rankine–Hugoniot (RH) jump conditions express the conservation of mass, momentum, energy, and magnetic flux of a magnetized fluid heated by a shock. A coordinate system was constructed in the shock frame such that $\hat{\boldsymbol{z}} = \hat{\boldsymbol{n}}$. The $\hat{\boldsymbol{x}}$ component was set parallel to the component of $\boldsymbol{B}_{\rm up}$ tangent to the shock surface, and $\hat{\boldsymbol{y}}$ completes the right-handed set. All RH jump conditions are referenced to this system, which is different for each shock. We decompose the magnetic fields and velocities as

$$\boldsymbol{B}_{\rm up/down} = B_k\hat{\boldsymbol{z}} + \boldsymbol{B}_l, \quad (9)$$

$$\mathbf{v}_{\rm up/down}^{\rm (sh)} = v_k\hat{\boldsymbol{z}} + \mathbf{v}_l \quad (10)$$

with the magnitudes $|\boldsymbol{B}_{\rm up/down}| = B$ and $|\mathbf{v}_{\rm up/down}^{\rm (sh)}| = v$. The subscripts l and k indicate quantities tangent and normal to the shock surface, respectively. The energy flux jump condition is

$$F_{\rm TOT}^{\rm up}|_{h_s=0} - F_{\rm TOT}^{\rm down} = \left[v_k\left(\rho_g h_g + \frac{1}{2}\rho_g v^2 + \sum_s \rho_s h_s\right) + \frac{1}{4\pi}(v_k B^2 - B_k(\mathbf{v}\cdot\boldsymbol{B}))\right]|_{h_s^{\rm up}=0} = 0, \quad (11)$$

where $F_{\rm TOT}^{\rm up/down}$ are the total fluxes of energy density upstream and downstream, respectively, [ ] indicates the difference between upstream and downstream quantities, and the subscript g denotes thermal gas quantities.[9] For later reference, we define the kinetic energy flux $F_{\rm KIN} = v_k\rho_g v^2$, the enthalpy flux $F_{\rm THERM} = v_k\rho_g h_g$, and the magnetic energy fluxes $F_{\rm MAG,1} = v_k B^2/(4\pi)$ and $F_{\rm MAG,2} = -B_k(\mathbf{v}\cdot\boldsymbol{B})/(4\pi)$. The normal momentum jump condition is

$$\left[\rho_g v_k^2 + P_g + \sum_s P_s + \frac{B_l^2}{8\pi}\right]|_{h_s^{\rm up}=0} = 0. \quad (12)$$

As mentioned above, the energized particle fluxes can rise steeply (quasi-exponentially) before the shock time. These particles originate downstream very close to the shock; some then diffuse upstream. Adding these particles to the upstream term of the jump conditions double-counts the energy/momentum of energetic particles, and misplaces into the upstream energy/momentum that likely originated downstream. Thus, only the downstream portion of the jump conditions includes $\sum_s \rho_s h_s$ and $\sum_s P_s$.

3.2. PSP Shock

The PSP shock on 2020 November 30 at 18:35 UT (Mitchell et al. 2021) is not cataloged in the CfA database, nor are precomputed shock/background plasma parameters available. The $\theta_{\rm Bn}$ is estimated to be $\sim 60°$ (Giacalone et al. 2021). Using polarization data from the Radio Frequency Spectrometer of the FIELDS instrument on board PSP (Bale et al. 2016), upstream waves seem to be close to field-aligned, which would be consistent with electrostatic Langmuir waves.[10] The low frequency (18.75 kHz) corresponds to a density of $\sim 4.3\ \rm cm^{-3}$. The spacecraft spatial orientation at the time of the shock passage made it impossible to accurately determine the shock speed and the downstream proton thermal speed using the Solar Wind Electrons Alphas & Protons (SWEAP) instrument (Kasper et al. 2016); reasonable values to assume seem to be $\sim 900\ \rm km\ s^{-1}$ and $40\ \rm km\ s^{-1}$, respectively. The PSP/FIELDS downstream magnetic field, which was obtained from the CDAWeb database, averaged over 10 minutes, is ~ 36.7 nT. We can infer the downstream number density by using the slopes of sections of the time-averaged particle energy spectra, assumed to be power laws from EPI-Hi and

[9] The downstream enthalpy flux of the energized particle species s in Equation (8), $h_s\rho_s v_k$, corresponds to the term $(5/2)PU$ in Giacalone et al. (1997).

[10] Dr. M. Pulupa, private communication.

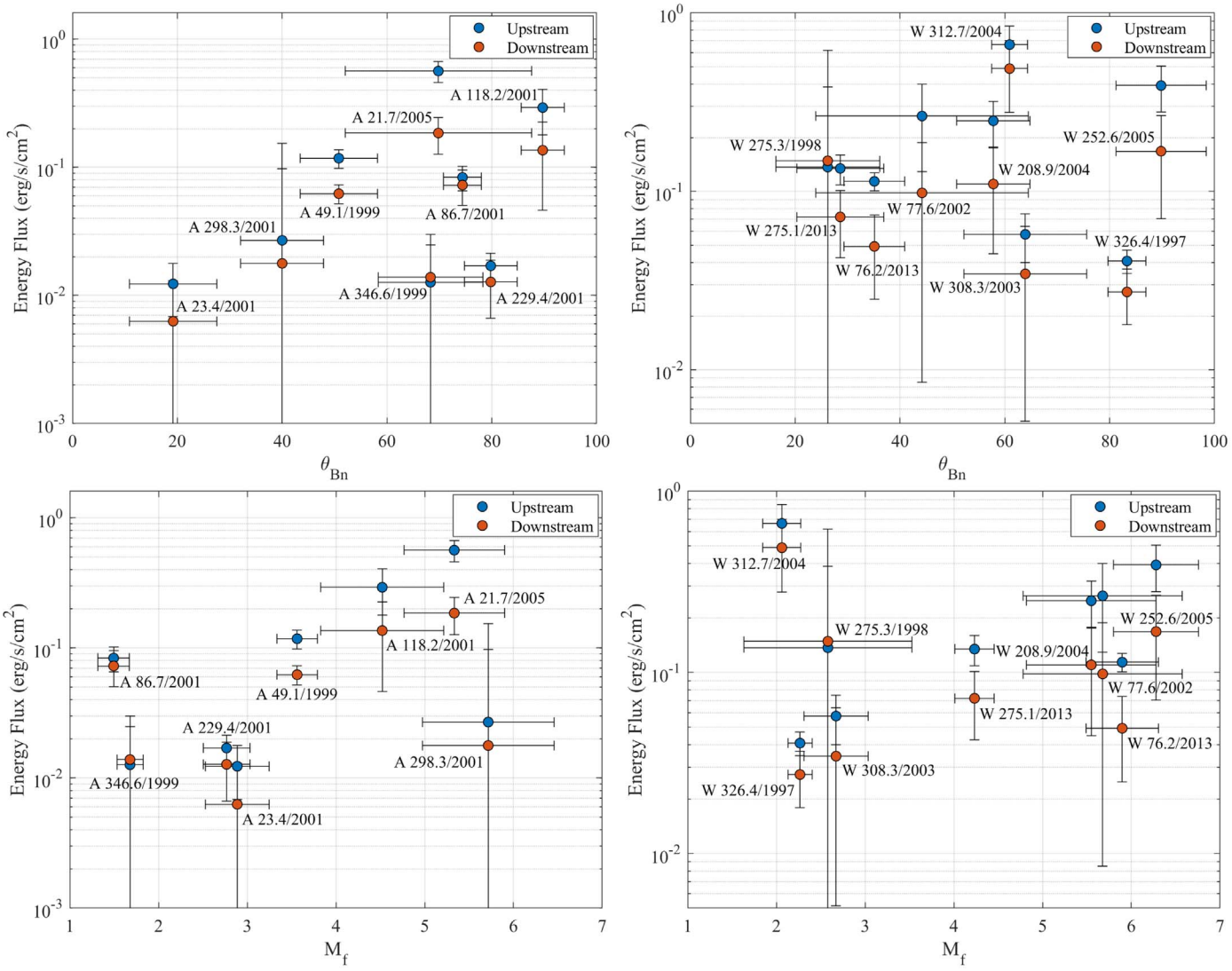

Figure 2. Upstream (blue) and downstream (red) energy fluxes at each shock with 1σ error bars for a 1 hr pre- and post-shock interval. The left and right panels correspond to ACE and Wind, respectively. The top row is plotted as a function of θ_{Bn} and the bottom as a function of M_f. Energized particle fluxes are included only in the downstream values to avoid contamination from particles diffusing from downstream (see Section 4). Particle fluxes are averaged for 1 hr beginning 1 minute after the shock time.

EPI-Lo measurements. In particular, EPI-Lo fluxes were averaged for 1 hr after the shock passage, constituting 12 samples of 5 minute duration each, after the fluxes reached a clear plateau about 20 minutes after the shock time. The EPI-Hi data are unavailable for about 10 hr after the shock but still show enhancement over background. We averaged the first two available fluxes in each energy bin, which corresponds to a period of 2 hr. In the assumption of linear DSA, the compression ratio is then

$$\frac{n_{\rm down}}{n_{\rm up}} = \frac{q}{q-3}, \tag{13}$$

where q is the absolute value of the power-law index. Averaging the slopes of three regions of the spectra, we obtain a reasonable ratio of 3.1. We compute a total downstream energy flux of $\sim 9.2\,{\rm erg/s/cm^2}$, roughly an order of magnitude larger than that for the ACE and Wind shocks (see results in Section 4). However, with these data uncertainties, we are unable to accurately verify the overall energy conservation.

3.3. Error Propagation

Particular attention has been paid to calculate the errors on each quantity appearing in the jump conditions (Equations (11) and (12)), as well as on the fraction of the total energy in downstream suprathermal and energetic particles. For each shock, we generated 10^5 sample shocks with all parameters randomly perturbed according to a normal distribution having as mean and standard deviation the values provided in the CfA database. These shocks were individually analyzed and the overall uncertainties on our results determined using the standard deviations. Therefore, the standard deviations calculated herein account for experimental sources of error.

4. Results

4.1. Energy Partition among Plasma Components

Figure 2 plots the energy flux upstream and downstream ($\mathbf{F}^{\rm up}_{\rm TOT}|_{h_s=0}$ and $\mathbf{F}^{\rm down}_{\rm TOT}$, Equation (11)) as a function of $\theta_{\rm Bn}$ (top panels) and M_f (bottom panels) for a 1 hr pre- and post-shock

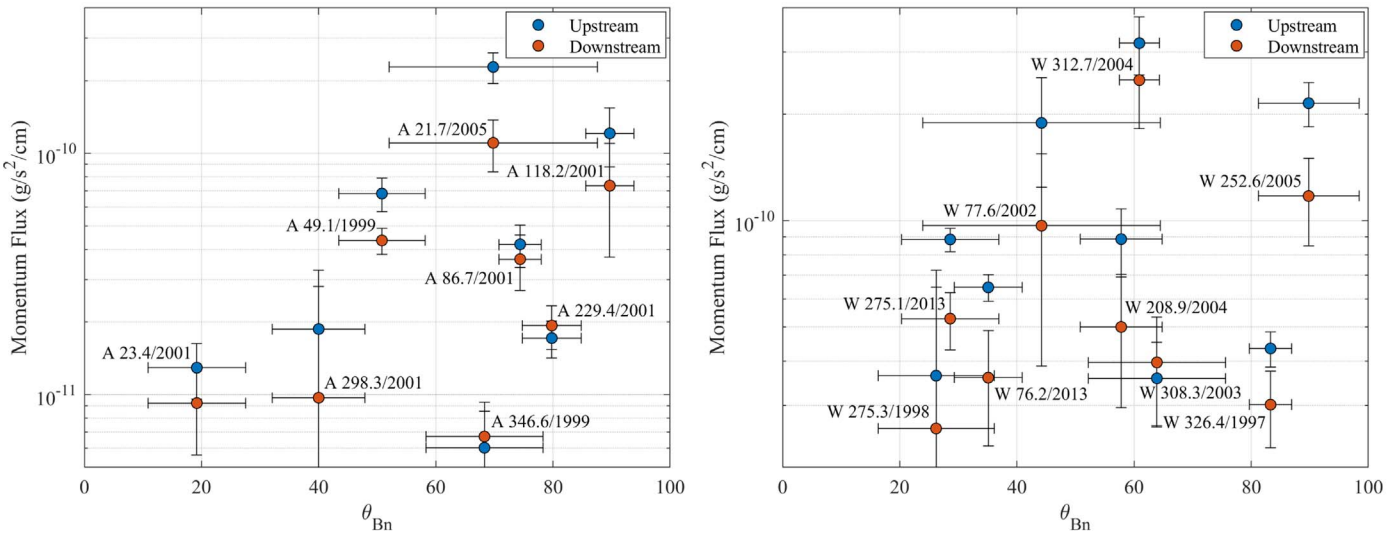

Figure 3. Upstream (blue) and downstream (red) normal momentum fluxes at each shock as a function of θ_{Bn} with 1σ error bars. The left and right panels correspond to ACE and Wind, respectively. Energized particle energy fluxes are included only in the downstream region. One hour averages offset by 1 minute from the shock times were used for particle flux determination.

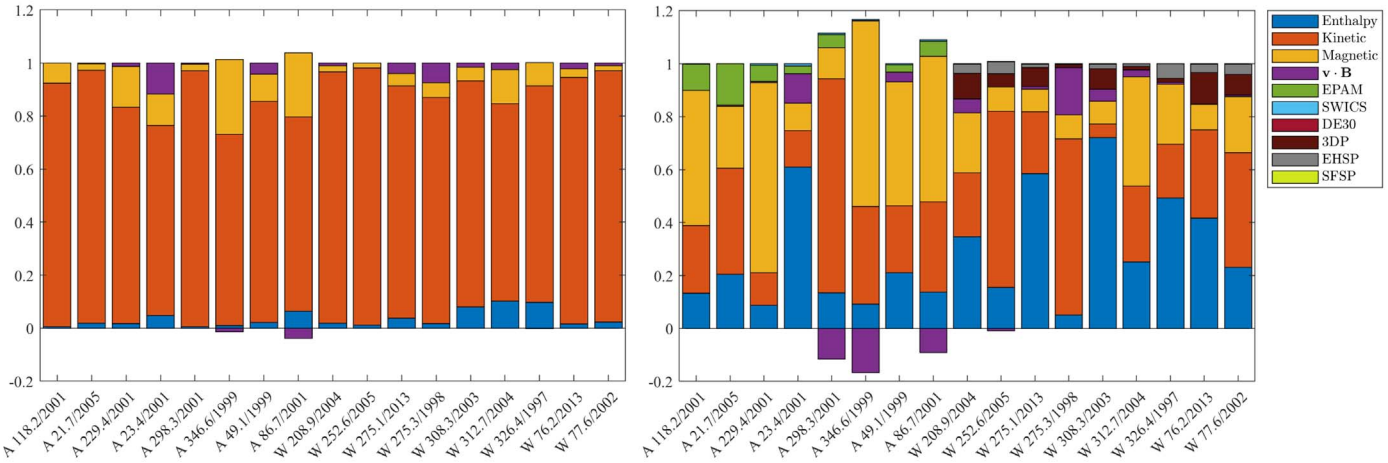

Figure 4. By comparing, for the ACE and Wind shocks, the energy partition in the upstream (left panel) with the downstream (right panel), the efficient conversion of the shock kinetic energy (F_{KIN}/F_{TOT}, red) into the plasma enthalpy (F_{THERM}/F_{TOT}, blue), magnetic pressure ($F_{MAG,1}/F_{TOT}$ yellow), the $\mathbf{v} \cdot \boldsymbol{B}$ term ($F_{MAG,2}/F_{TOT}$, purple), and energized particles ($v_k \rho_s h_s / F_{TOT}$, all other colors) is apparent. The total energy flux has been normalized to 1 and the 1 minute offset bins for both upstream and downstream as described in Section 4.3 were used.

interval. Six of the eight ACE shocks (23/2001, 298/2001, 346/1999, 86/2001, 229/2001, and 118/2001) and five of the nine Wind shocks (326/1997, 275.3/1998, 77.6/2002, 312/2004, and 308/2003) show a matching of upstream and downstream energy fluxes within 1σ errors. Only ACE 21/2005 does not match within 2σ. Figure 3 shows the normal momentum RH jump conditions (Equation (12)), exhibiting the same pattern: the shocks that match within 1σ in energy flux do likewise in momentum flux, except for Wind 326/1997.

Figure 4 shows the values of the different energy flux components for each shock normalized to the total energy flux, in the respective region, upstream (left panel) and downstream (right panel). The upstream ram pressure (red), which dominates the energy flux, is efficiently converted downstream into other components by the shock, mostly magnetic (yellow) and thermal (blue). Wind events show an energized electron energy fraction (EHSP + SHSP, gray + lime) not negligible with respect to that of ions (dark red); the same cannot be concluded about the ACE events due to the large electron energy cutoff of DE30 data.

All ACE events (except 23.4/2001 and 298.3/2001, which have the smallest θ_{Bn}) and all Wind events show a large magnetic energy fraction downstream, as well as a large fraction increase, suggesting that the field might undergo a downstream amplification beyond compression, possibly due to upstream density inhomogeneities (Giacalone & Jokipii 2007; Fraschetti 2013). Comparably large magnetic fractions are not found at the two quasi-parallel events. For the shocks ACE 298/2001, 346/1999, 86/2001, and the Wind shocks 252/2005, 326/1997 the term $F_{MAG,2}$ is negative, resulting in normalizations greater than one.

4.2. Energetic Particle Fractions

For the ACE/Wind shocks, the fractions of energy drained into the suprathermal/energetic particle populations are summarized in Figure 5. Note that the energy fraction is

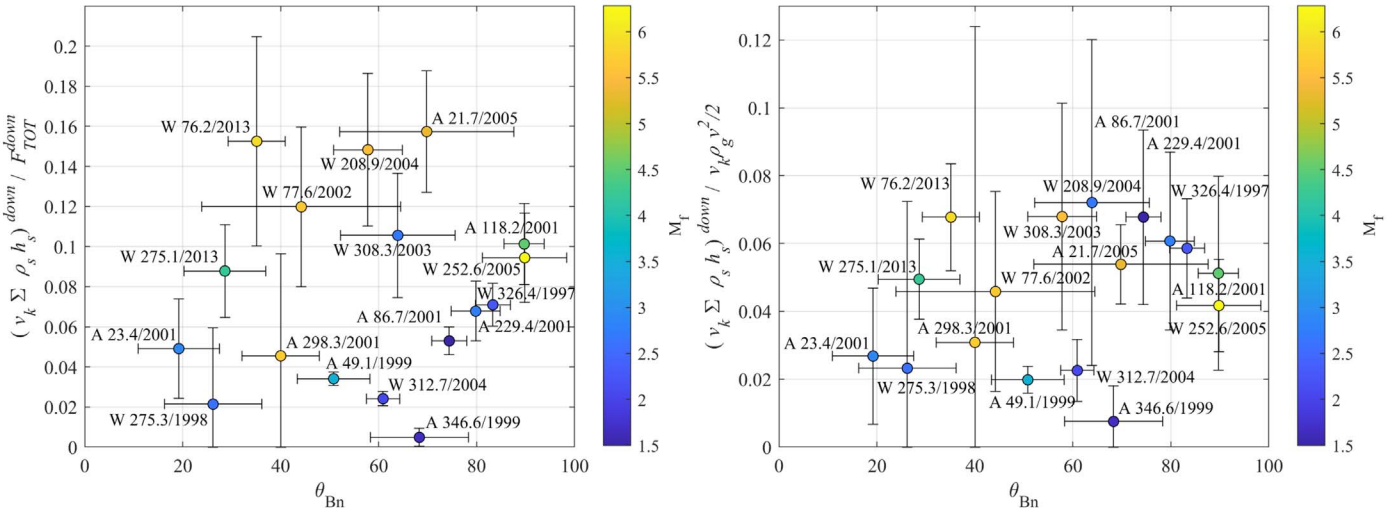

Figure 5. Left: ratio of downstream energy flux of energized particles (protons + electrons, $(v_k \sum \rho_s h_s)^{\rm down}$) to the total downstream energy flux ($F_{TOT}^{\rm down}$) as a function of $\theta_{\rm Bn}$ for both ACE and Wind. Spacecraft data show no decrease in the particle partial pressure with $\theta_{\rm Bn}$ for a given M_f, that is color-scaled by the right bar. For the ACE shocks, the EPAM, SWICS, and DE30 energies are summed, and for the Wind shocks, the 3DP, EHSP, and SFSP are summed. Right: ratio of downstream energy flux of energized particles (protons + electrons, $(v_k \sum \rho_s h_s)^{\rm down}$) to the upstream ram pressure flux $(\rho_g v^2 v_k/2)^{\rm up}$. Again, no trend of decrease of energized particles contribution as $\theta_{\rm Bn}$ increases is measured.

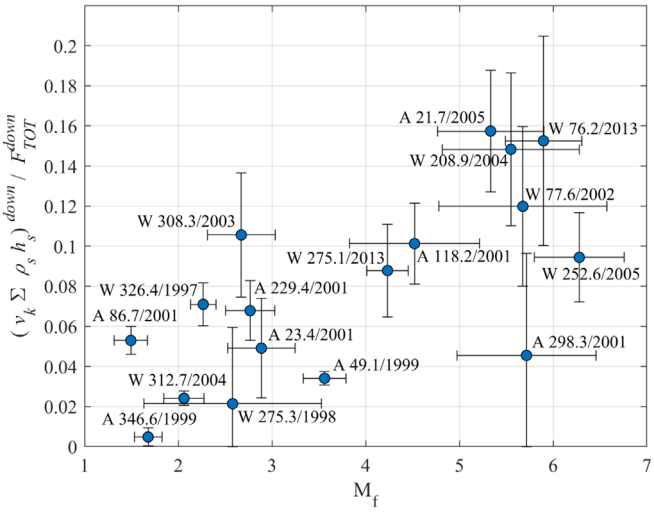

Figure 6. Ratio of downstream energy flux of energized particles (protons + electrons, $(v_k \sum \rho_s h_s)^{\rm down}$) to the total downstream energy flux ($F_{TOT}^{\rm down}$) as a function of M_f.

defined in Figure 5, left panel, as the ratio of downstream enthalpy flux of energized particles (protons + electrons) $(v_k \sum \rho_s h_s)^{\rm down}$ to the total downstream energy flux $F_{TOT}^{\rm down}$, differently from the efficiency used, e.g., by Ellison & Moebius (1987) or Giacalone et al. (1997), that is the ratio of downstream enthalpy flux of energized particles to the upstream kinetic energy flux $(\rho_g v^2 v_k/2)^{\rm up}$ (Figure 5, right panel). For the former definition, the fractions span from 0.48% to 16%, and for the latter, the fractions range from 0.75% to 7.2%. The reason for comparing different normalizations is that some events show a nonnegligible fraction (up to 30%) of incoming nonkinetic (e.g., magnetic) energy (see Figure 4); thus, the use of the kinetic energy only would lead to an underestimate of the energy available for particle acceleration. The upstream energy fluxes shown in Figure 2 exceed the downstream energy fluxes for all but two shocks (ACE 346/1999 and Wind 275/1998), despite being equal within 1σ (see Section 5.2); as a result, the ratios in the right panel are typically smaller than those in the left panel. Regardless of the normalization chosen in the two panels of Figure 5, the lack of correlation of the energetic particle partial pressure with $\theta_{\rm Bn}$ is manifest: no evidence emerges that the partial pressure of the energized particles decreases with increasing $\theta_{\rm Bn}$. For the PSP shock, we find that energized protons (combining EPI-Lo and EPI-Hi) constitute 7.7% of the total downstream energy flux, in agreement with our ACE and Wind results. We conclude that the energized particles fraction is consistent with $\lesssim$20%.

Not only does the energy fraction not decrease at large $\theta_{\rm Bn}$ for any given M_f; on the contrary, we found events with $\theta_{\rm Bn} \gtrsim 70^\circ$ and energy fractions as large as $\sim$10%, and having smaller relative errors than events with $\theta_{\rm Bn} \lesssim 70^\circ$. This result confirms with high accuracy longstanding in situ measurements that demonstrate that ions are efficiently accelerated at quasi-perpendicular shocks (e.g., Reames 2012), a result corroborated by the most recent particle-in-cell (PIC) simulations in van Marle et al. (2018); see also the review on PIC simulation findings on the wave modes excited upstream of shocks (Pohl et al. 2020). Large-scale preexisting upstream magnetic turbulence is suggested to enhance the ion acceleration efficiency at quasi-perpendicular shocks by numerical simulations over a broad shock parameter range (Giacalone 2005; Fraschetti & Giacalone 2015) and models of in situ STEREO measurements (Fraschetti & Giacalone 2020). The results presented herein are open to such an interpretation. High-amplitude and high-frequency whistler waves excited by electrons in the shock layer (Katou & Amano 2019; Amano et al. 2020) and traveling upstream might also drive upstream turbulence. A number of electron-scale instabilities in the high plasma beta regime of intra-cluster shocks were studied in 2D PIC (Kim et al. 2021), suggesting that ion-scale waves are generated by distinct instabilities on longer timescales, partially overlapping with electron timescales.

Figure 6 shows the ratio of the downstream enthalpy flux of energized particles to the total downstream enthalpy flux as a function of M_f. The results display a bias toward higher particle energy fractions for high-M_f shocks. Generally, this is expected

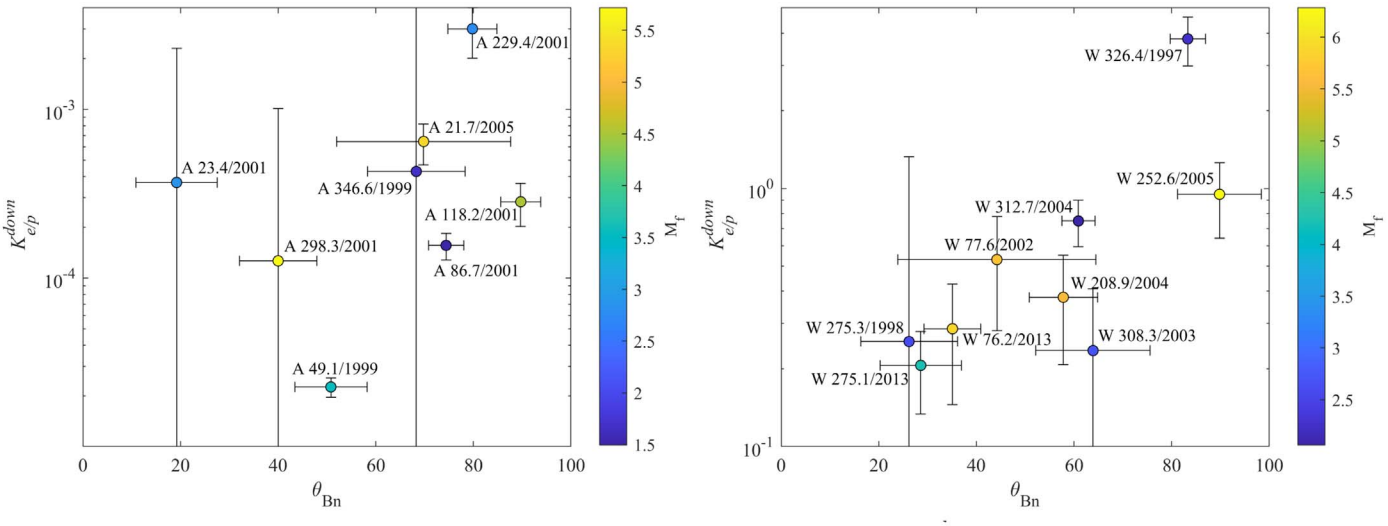

Figure 7. Ratio of the downstream energized electron-to-proton energy flux $K_{e/p}^{\rm down}$ as a function of $\theta_{\rm Bn}$ for ACE (left panel) and Wind (right panel). The ratio for ACE shocks is roughly two to three orders of magnitude smaller than that of the Wind shocks, which might indicate that electrons with energies < 38 keV (the lower bound of ACE/DE30) contribute a nonnegligible fraction. Data below this energy are unavailable for ACE, while EHSP extends to the energy cutoff herein used for Wind.

in standard DSA theory since the plasma density compression ratio, which determines the power-law slope of the high-energy tail of the distribution, increases with M_f to its maximum value of 4. Moreover, the acceleration rate increases with shock speed (and, hence, M_f). Thus, we expect more high-energy particles with increasing M_f. A notable exception in Figure 6 is ACE 298/2001, possibly affected by one of the largest errors in the downstream energy fraction of our sample.

The downstream energized electron-to-proton energy flux ratio $K_{e/p}^{\rm down}$ is displayed in Figure 7. Remarkably, a mismatch in the order of magnitude between ACE and Wind is found, where the former would be closer to the expected electron-to-proton post-shock temperature ratio derived from the collisionless jump conditions (given by electron-to-proton mass ratio). However, the latter is closer to the PIC-simulated high-energy tail of the spectra for quasi-parallel shocks (Kato 2015) and to the Payload for Antimatter Matter Exploration and Light-nuclei Astrophysics$\sim 1-600$ GeV electron-to-proton flux ratio cumulatively measured at Earth (Adriani et al. 2011a, 2011b). The low value of $K_{e/p}^{\rm down}$ for ACE events might be due to the small increase in the DE30 electron intensity at the shocks not shown here, which is entirely absent for some events. Also, DE30 fluxes have an elevated instrumental background in the events considered, leading to the large error bars in Figure 7. Contrasting all other shocks in this study, in Wind 326/1997, the energy in downstream energized electrons (EHSP) exceeds that in downstream energized (3DP) protons; for Wind 252/2005, the relative contributions match within 1σ. Both of these results are likely due to missing energy components, which we discuss more in Section 5.2.

4.3. Time-series Particle Energy Flux

The effect of shifting the particle flux averaging time intervals after the shock time is summarized in Figures 8 and 9. The time intervals were offset in 10 minute steps between 10 and 180 minutes after the shock time with an additional offset beginning 1 minute after the shock. A minimum of 1 minute was chosen to reduce the effects of strong fluctuations in particle fluxes often seen immediately after a shock, and the 1 hr duration further reduces the impacts of such high-frequency variations. Since the SWICS data have a 12 minute cadence, only SWICS fluxes that fell strictly within the 1 hr windows were averaged.

In reference to Figure 9, two shocks, ACE 118/2001 and 298/2001, display a constant combined proton and electron energy flux fraction up to at least 3 hr downstream, whereas other events exhibit a variety of time dependencies (variations in the latter shock are likely hidden by the large errors, however). ACE 21/2005 and 49/1999 decay fastest, with the flux at 1 hr being just a third of that found immediately following the shock. ACE 86/2016, and Wind 308/2003, 326/1997, 275.1/2013, and 76/2013, drop between 15% and 40% over the same time. The steep drop of the downstream intensity profiles might be affected by efficient downstream particle escape (Fraschetti 2021). For ACE 346/1999, however, the fraction increases with time by $\sim$50%. This event precedes a much larger shock by about 0.2 days and was thus caught in the quasi-exponential upstream rise of the subsequent shock. ACE 229/2001 dips by 35% at $\sim$40 minutes behind the shock before regaining 80% of its initial flux at $\sim$90 minutes. ACE 23/2001 is maximum about 60 minutes after the shock, growing about 150% relative to the value at the shock. This maximum is marked by a 300% jump in the magnetic pressure (not shown here) and an abrupt rotation of the field, possibly the result of the spacecraft passing through a magnetic structure, e.g., a flux tube. In addition, the shock time is marked by a $\sim$15 minute spike (Lario et al. 2003) in particle intensity, twofold enhanced from the downstream intensity. This local enhancement is followed by an unusually slow rise in proton fluxes, meaning our 1 minute offset, 1 hr duration averaging interval includes the latter half of the spike but precedes the broader peak that occurs 1 hr after the shock. Such a peak might be due to downstream magnetic reconnection, invoked to explain the peaks in energetic proton fluxes about 6 days after the Voyager 2 crossing of the heliospheric termination shock (Zank et al. 2015). No Wind shocks exhibit late downstream peaking. Since in most cases electrons constitute a significantly smaller energy fraction than protons, these trends apply to the proton-only time-series as well. DE30 electrons track EPAM protons in all

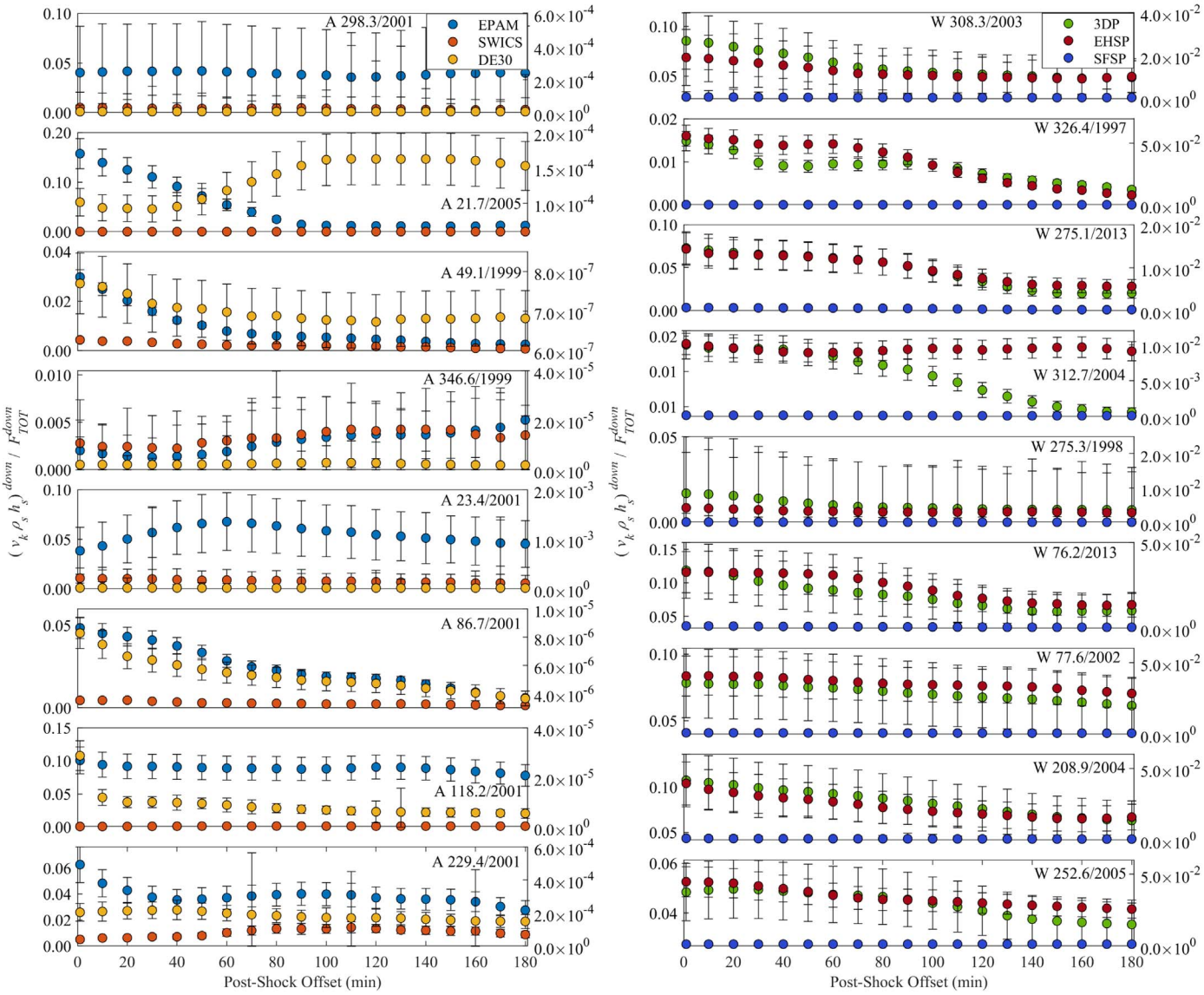

Figure 8. Left: time dependence of the 1 hr averaged downstream energy fraction of energized protons and electrons from each instrument. The averaging interval was offset from the shock time by 1 minute, and then shifted in 10 minute steps between 10 and 180 minutes (see Section 4). In the ACE plots, EPAM suprathermal ions (blue), SWICS ions (red), and DE30 electrons (yellow) are shown. The left axis scale corresponds to EPAM and SWICS, and the right to DE30. Right: for Wind, 3DP protons (green), EHSP electrons (red), and SFSP electrons (blue) are shown. The right axis scale corresponds to 3DP, and the left to EHSP and SFSP. In most cases, there is a clear decrease in the particle energy fraction about 1 hr after the shock.

discernible cases except for ACE 21/2005, where it grows to about 200% its post-shock value ∼2 hr downstream.

The right panels of Figure 8 show that SFSP electrons have negligible contributions to the energy fractions at all Wind shocks. Furthermore, large errors on the associated energy fluxes make any attempts to discern trends in this energy range unfruitful. The EHSP fraction tracks closely that of the 3DP protons for all shocks except for Wind 312/2004, for which the fraction remains relatively unchanged across the 3 hr interval.

The total particle partial pressures (combining electrons and protons) over all of the instruments herein used are plotted in Figures 10 (ACE) and 11 (Wind), for both upstream and downstream plasmas. In most cases, except for ACE 49/1999 and Wind 275.1/2013, the particle partial pressure downstream exceeds its value upstream, even at the closest pre-shock sampling point. The magnetic field components and absolute value (not shown here) have no discernible upstream features that could explain the atypical behavior of these two shocks. We note two types of upstream behaviors: most events show a gradual monotonic increase over the entire 3 hr interval toward the shock time whereas two events (ACE 346/1999 and Wind 312/2004) exhibit oscillatory behavior. The peak in proton flux ∼100 minutes prior to the shock ACE 346/1999 does not correspond to evident features in the magnetic strength (e.g., a cavity) so it might be affected by other large-scale effects. The enhancement may result from magnetic connection of the spacecraft with a spatially distant region that the shock has already passed. The downstream partial pressures follow the downstream energy fractions in Figure 9. The shock Wind 275.1/2013 is atypical because the partial pressure nearly flattens for the 3 hr before the shock and decreases at the shock. This behavior is due to an unusually large upstream flux of protons in the highest four 3DP energy bins, which exceeds that in the downstream. In other words, the passage of the

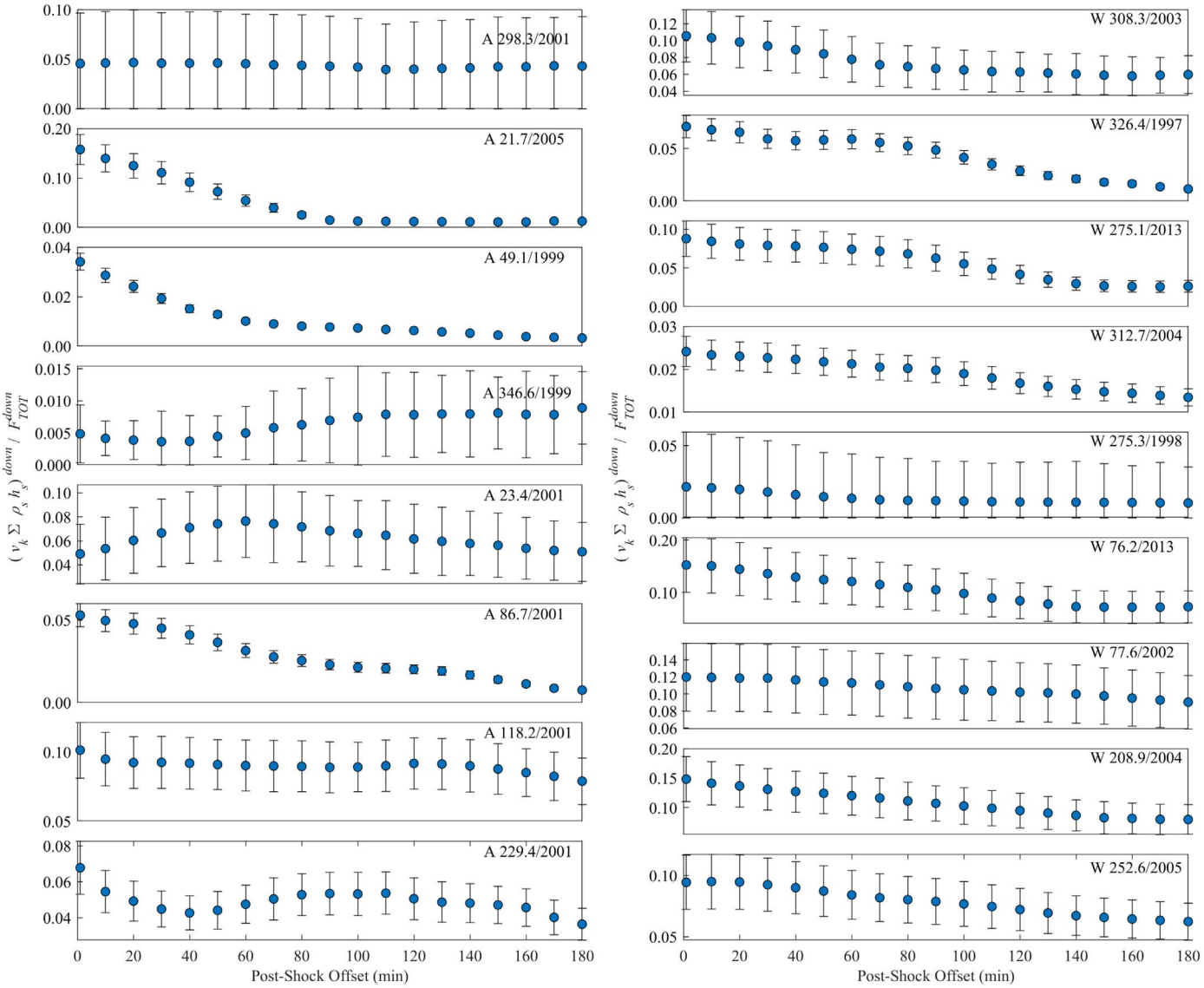

Figure 9. For ACE (left) and Wind (right), the change as a function of time of the 1 hr averaged downstream energy fraction of energized protons and electrons summed over all instruments is plotted; the time intervals are defined as explained in Figure 8. In most cases, there is a clear decrease in the particle energy fraction about 1 hr after the shock.

shock increased the number of protons between 67.3 keV and 1.02 MeV while decreasing those between 1.02 MeV and 6.76 MeV. No significant wave-activity is reported in the 3 hr prior to the shock time by the Wind/Magnetic Field Investigation. Similarly, we observe a drop in particle pressure after the shock ACE 49/1999, but contrasting the Wind shock, the profile rises and falls quasi-exponentially upstream and downstream, and no atypical features are found in the particle fluxes.

5. Discussion

5.1. Analysis Time Interval

Earth bow shock crossings by the Magnetospheric Multiscale (MMS) spacecraft were used by Hanson et al. (2020) to minimize the error in the RH jump conditions: the upstream and downstream time windows were varied to determine shock parameters including θ_{Bn}, the shock normal, and the shock speed with a very high time resolution. The change in the upstream and downstream shock parameters was found to be modest within the selected time window (a 1 minute window shifted within 5–10 minutes of the shock time, corresponding to the sampling closest to the shock in Figures 8, 9, 10, 11 herein). Our analysis uses a determination of shock parameters over a longer time interval (c.a. 10–20 minutes via the CfA database) and applies a larger window (1 hr) out to much larger distances from the shock (3 hr) than MMS in order to capture the contribution of energized particles streaming away from the shock. The energetic particle intensity profiles are observed to rise over the far upstream background as early as 3 hr before the shock for the quasi-parallel geometry. Thus, the determination of energy conservation performed herein relies on stable parameters determined from 1 minute to 3 hr after the shock time. The downstream time window approaches the shock as close as possible to capture the freshly energized particles.

The effect of large-amplitude fluctuations in the particle intensity immediately past the shock, present in some events, on the calculated partial pressure and the energy conservation

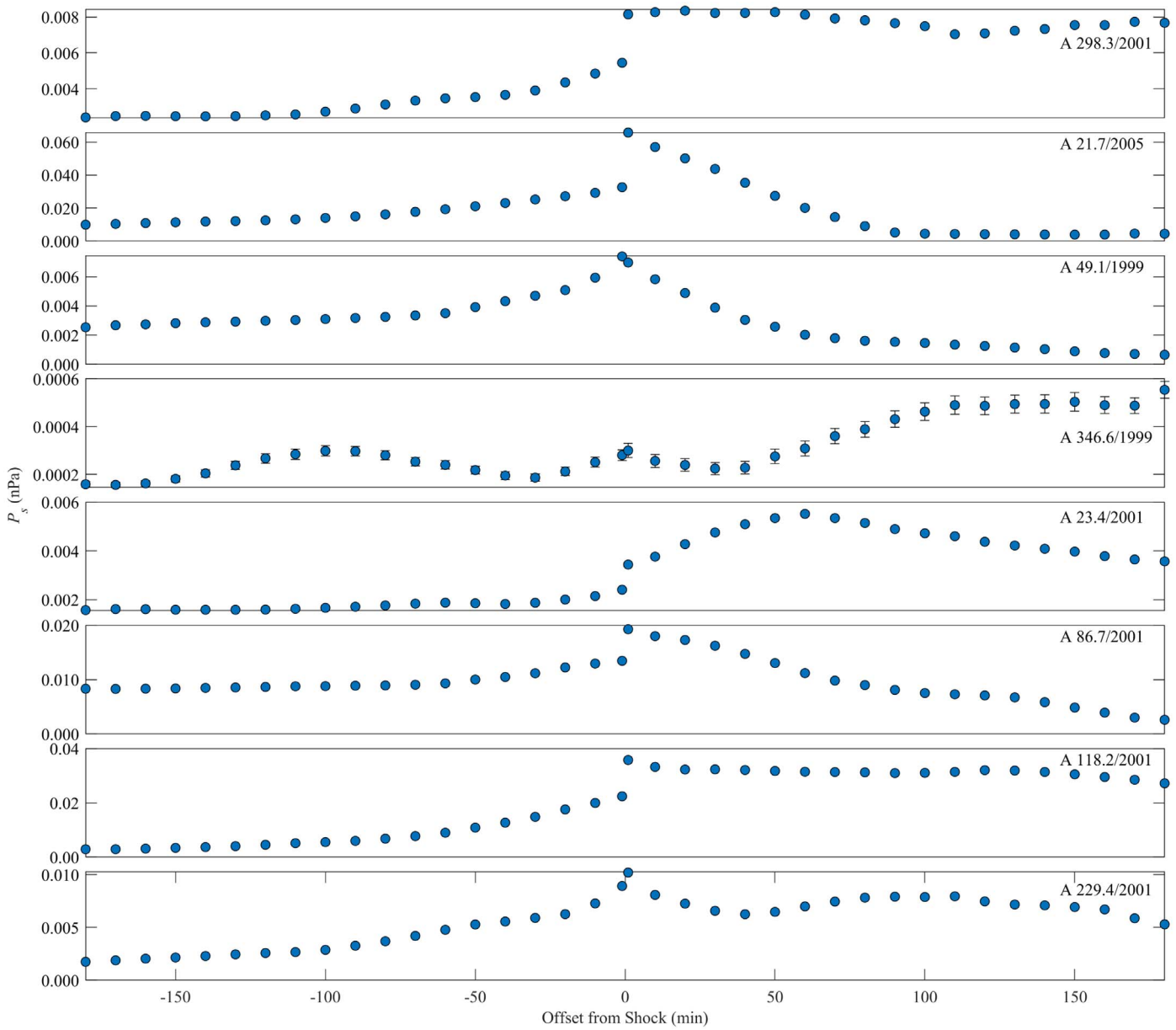

Figure 10. For each ACE shock, the change as a function of time of the 1 hr average total energized particle pressure is plotted; the time intervals are as explained in Figure 8, and are here combined upstream and downstream.

within 1σ errors is smeared out by the long time interval used in our analysis. In most cases, the upstream partial pressure of energized particles immediately preceding the shock does not exceed 70% of that immediately downstream.

5.2. Missing Energy Components

The upstream and downstream energy fluxes, including the energized particle pressure only in the downstream region, for 11 of the 17 ACE/Wind shocks in our sample, match within 1σ, and all but one (ACE 21/2005) match within 2σ. Moreover, for all but two shocks (ACE 346/1999 and Wind 275/1998), the upstream energy flux exceeds that downstream (although still within 1σ errors), implying missing energy components. Indeed, the Wind 3DP instrument ranges from a minimum energy of 67.3 keV; hence, the proton energy ranges from 10.7 keV – 67.3 keV (for the slowest shock) to 57.4 keV – 67.3 keV (for the fastest shock) are unaccounted for. As we mentioned above, the PESA-Hi fluxes, which range from 400 eV to 19.1 keV and therefore would reduce the range of missing energies, are not included in the ion partial pressure due to large errors. Since energy spectra generally increase toward lower energies, the contribution from this energy range is expected to be nonnegligible, thereby explaining at least part of the unaccounted downstream energy.

5.3. Electron-to-proton Ratio

The $K_{e/p}^{\rm down}$ values for the ACE shocks ($\lesssim 10^{-3}$) are likely to be a considerable underestimate due to the lack of electron data below 38 keV. Conversely, for electrons, the Wind/EHSP data product extends down to 136 eV, but protons below 67.3 keV

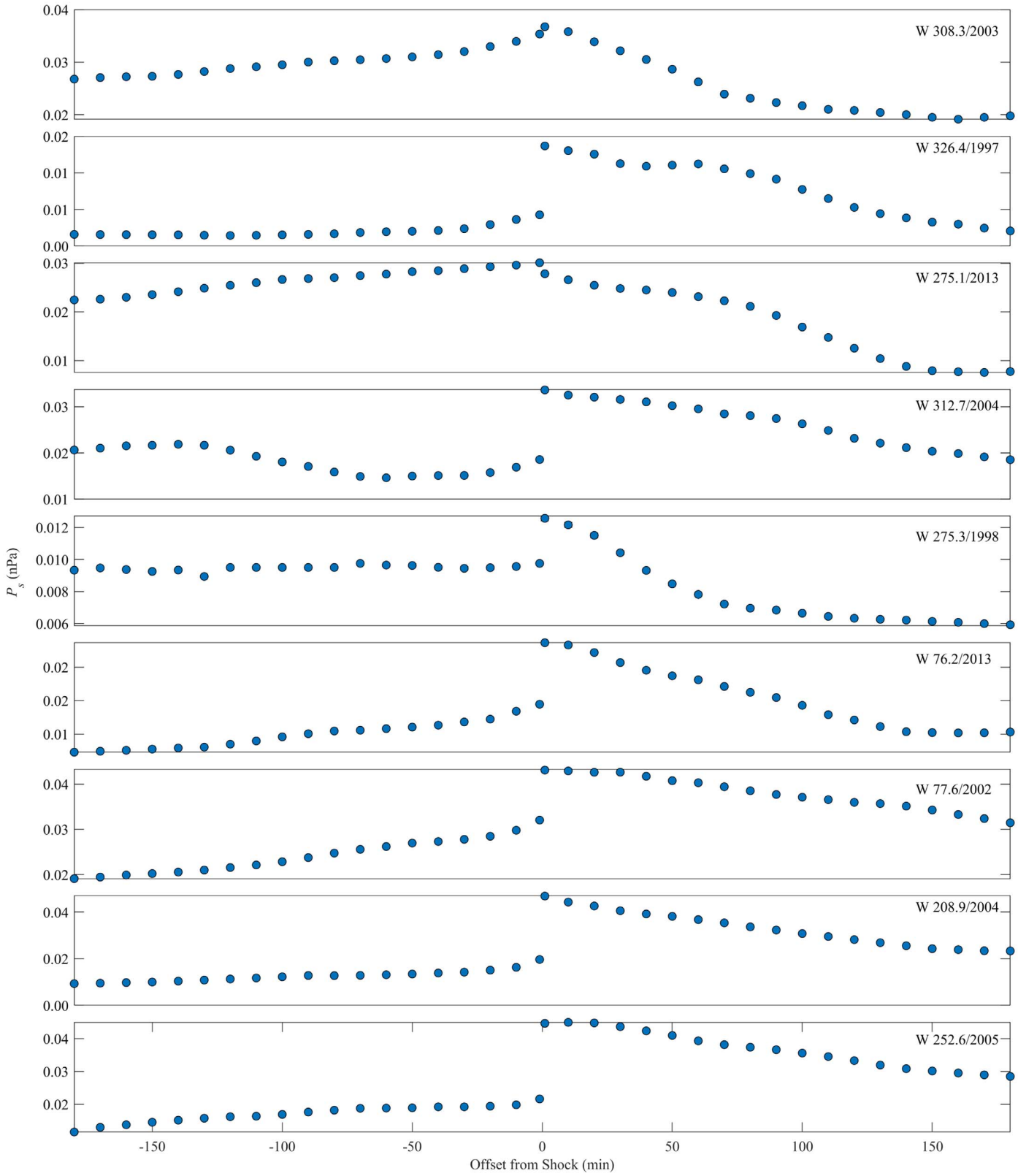

Figure 11. Same as Figure 10 for Wind shocks.

are unaccounted for; whereas SWICS covers this energy range for ACE. Certainly a nonoptimized calibration of the electron and proton instrument responses can also lead to a mismatch between the $K_{e/p}^{\mathrm{down}}$ inferred from ACE and Wind measurements. The lack of lower-energy protons (combined with the full electron energy coverage) for Wind might explain $K_{e/p}^{\mathrm{down}} > 1$ in Wind 326/1997, and $K_{e/p}^{\mathrm{down}} \sim 1$ for Wind 252/2005. For all Wind shocks, the ratio is surprisingly close to

equipartition and as expected trends upward with magnetic obliquity: even in the suprathermal range, scatter-free electrons outrun and repeatedly cross the shock, thereby being energized by following meandering field lines as pointed out in Jokipii & Giacalone (2007).

As for $K_{e/p}^{\rm down}$ exceeding unity in the highly perpendicular event Wind 326/1997 ($\theta_{\rm Bn} = 83.3°$), an energy transfer from protons to electrons can be ruled out due to the low collisionality of the system: the collisional frequency for energy transfer of a 100 eV electron over the thermal protons is $\nu_{ep} \sim 3.9 \times 10^{-6} (n_p/{\rm cm}^{-3}) \Lambda \, (\epsilon/{\rm eV})^{-3/2} \, {\rm s}^{-1}$ that for $\Lambda \sim 20$ and $n_p \sim 3 \, {\rm cm}^{-3}$ (at 1 au) yields a timescale (~2 months) much longer than a Sun-to-Earth shock lifetime. An alternative explanation could be efficient electron upstream pre-heating due to trapping by a two-stream instability between incoming electrons and reflected ions (Scholer et al. 2003). Electron heating can also arise, only at oblique shocks, from energy transfer between specularly reflected ions and field-aligned electrons via resonant interaction with lower hybrid waves, as measured in laboratory experiments (Rigby et al. 2018). The necessary wave-particle analysis is beyond the scope of this work. Despite focusing on the peak of the velocity distribution, i.e., orders of magnitude below the range explored herein, Wilson et al. (2020) found that, for 52 Wind IPs, the absolute value of, and change in, the thermal/suprathermal electron pressure upstream/downstream is often comparable to or larger than that of ions. We show that the near-to-equipartition regime extends to the suprathermal/energetic particle regime, emphasizing the importance of electrons in the shock dynamics, and the necessity of a fully kinetic numerical approach.

The values of $K_{e/p}^{\rm down}$ for Wind shocks in Figure 7 are also one to three orders of magnitude higher than those estimated for high Mach number SNR shocks ($\sim 10^{-4}$–10^{-2}), as deduced from galactic cosmic ray fluxes measured at Earth, multiband X-ray/gamma-ray spectra of young SNR, and simulations (e.g., Berezhko et al. 2009; Morlino et al. 2009; Yuan et al. 2012). PIC simulations of SNR shocks suggest that, at high obliquity, electrons drive upstream turbulence prior to significant ion acceleration: again, fully kinetic simulations are needed to determine ion energy spectra (Bohdan et al. 2020; Kim et al. 2021). We note that low Mach number (~ 2–4) shocks in galaxy clusters (Vazza et al. 2015) are also consistent with the near-equipartitioning of (relativistic) electrons and protons or electron acceleration efficiency exceeding protons ($K_{e/p}^{\rm down} \sim 1$–100).

6. Conclusions

We have studied particle acceleration at 17 IPs crossed at 1 au by the ACE and Wind spacecraft and 1 shock crossed by PSP at 0.8 au. We have determined that electrons and protons energized by shocks at 1 au typically drain up to 10% of the upstream kinetic energy flux or up to 16% of the total downstream energy density, consistent with previous estimates inferred for shocks associated with energetic CMEs (e.g., Mewaldt et al. 2008; Emslie et al. 2012; Aschwanden et al. 2017) or high Mach number SNR shocks (e.g., Slane et al. 2014; Hovey et al. 2015; Bamba et al. 2018). The presumably strong shock crossed by PSP at 0.8 au is consistent with this estimate.

We have found no significant correlation between the energy fraction in energized particles and $\theta_{\rm Bn}$ for each given $M_f \lesssim 7$, in agreement with recent combined MHD-PIC simulations (van Marle et al. 2018); the energy fraction of energized particles does not decrease with $\theta_{\rm Bn}$ and grows with M_f. The events considered rule out, with unprecedented accuracy, that the acceleration efficiency, defined both with respect to the total downstream energy and to the upstream ram pressure, is significantly higher at low magnetic obliquity. Therefore, in situ measurements show that quasi-perpendicular shocks ($\theta_{\rm Bn} > 45°$) are not disfavored sites for efficient particle (i.e., both protons and electrons) acceleration with respect to quasi-parallel shocks ($\theta_{\rm Bn} < 45°$).

We have estimated the energized electron-to-proton energy ratio $K_{e/p}^{\rm down}$ in the suprathermal and energetic particle regime. For the ACE shocks, the instrumental electron energy range does not cover energies down to the DSA cutoff, yielding an underestimate of $K_{e/p}^{\rm down}$. For Wind shocks, the near-equipartition between the electron and proton partial pressures, possibly affected by an incomplete proton energy coverage, is considerably higher than that inferred for astrophysical shocks (typically 10^{-2}) and suggests that the role of electrons in the dynamics of shock waves and the generation of upstream turbulence cannot be neglected. The modeling of shock evolution in the inner heliosphere must include all components in the energy balance and cannot be limited to a hybrid approach, although several hybrid simulations are well-supported by in situ measurements (e.g., Giacalone et al. 1997).

The IPs analyzed in this paper were carefully selected on the basis of the errors in each term (background plasma as well as energized protons and electrons) of the RH jump conditions, resulting in a matching of upstream and downstream total energy fluxes within 1σ for 11 of the 17 analyzed shocks. The collected sample is representative of an extensive scan of the ACE/Wind databases. For the majority of other shocks in the ACE/Wind databases, over the entire M_f range, the errors on the shock speed and normal direction are too large to draw a conclusive statement on the relation between the obliquity and the fraction of total incoming energy transferred into energized particles.

The time dependencies of the downstream and upstream energized particle pressures revealed a variety of behaviors. For most events, the particle pressure rises monotonically before the shock and decays monotonically downstream, as suggested by models combining acceleration and escape (Fraschetti 2021). Two shocks in our sample exhibited particle pressures peaking 1–2 hr after the shock, potentially explained by late downstream magnetic reconnection (Zank et al. 2015) or the passage of the spacecraft through a magnetic flux tube. The long averaging interval used in this study (1 hr) effectively reduces the effects of fluctuations in the particle intensities, particularly those close to the shock. Due to these rapid variations, as well as events unrelated to the shock that nevertheless affect energized particle populations, surveying the particle fluxes on timescales of several hours both upstream and downstream is important to verify their source.

Possible avenues of future research include extending as much as possible the energy coverage in the particle flux data, thereby allowing for a more appropriate quantification of the total energy flux, as well as of $K_{e/p}$ and a better verification of the jump conditions. PSP and Solar Orbiter, for example, contain instruments capable of surveying broader energy ranges (e.g., Kasper et al. 2016; McComas et al. 2016; Owen et al. 2020; Rodríguez-Pacheco et al. 2020). Finally, shock crossings at multiple spatial locations equidistant from the Sun,

or pan-heliospheric monitoring of the time evolution of the particle pressure at a given shock by multiple spacecraft at distinct distances from the Sun, will certainly be topics of future studies.

This paper uses data from the Center for Astrophysics | Harvard & Smithsonian Interplanetary Shock Database (https://lweb.cfa.harvard.edu/shocks/). We thank Dr. M. Stevens for providing us with guidance on the database, Dr. M. Pulupa for suggestions on the PSP event, and Dr. L. Wilson III for help with Wind/PESA data. The material contained in this document is based upon work supported by a National Aeronautics and Space Administration (NASA) grant or cooperative agreement. Any opinions, findings, conclusions, or recommendations expressed in this material are those of the authors and do not necessarily reflect the views of NASA. This work was supported through a NASA grant awarded to the Arizona/NASA Space Grant Consortium. This work was also supported in part by NASA grant No. 80NSSC20K1283 as part of the Heliophysics System Observatory Connect Program. F. F. was supported, in part, by NSF under grant No. 1850774, and by NASA under grant Nos. 80NSSC18K1213, 80NSSC20K1283, 80NSSC21K0119, and the Chandra Theory Award Number TM0-21001X, issued by the Chandra X-ray Observatory Center, which is operated by the Smithsonian Astrophysical Observatory for and on behalf of NASA under contract NAS8-03060. J.G. was supported, in part, by NASA under grants 80NSSC18K1213, 80NSSC20K1283, and 80NSSC21K0119. D.L. acknowledges support from NASA HGI grant No. NNX16AF73G and the Living With a Star (LWS) programs NNH17ZDA001N-LWS and NNH19ZDA001N-LWS, as well as the Goddard Space Flight Center Heliophysics Innovation Fund (HIF) program.

ORCID iDs

Liam David https://orcid.org/0000-0003-1713-9466
Federico Fraschetti https://orcid.org/0000-0002-5456-4771
Joe Giacalone https://orcid.org/0000-0002-0850-4233
Robert F. Wimmer-Schweingruber https://orcid.org/0000-0002-7388-173X
David Lario https://orcid.org/0000-0002-3176-8704

References

Adriani, O., Barbarino, G. C., Bazilevskaya, G. A., et al. 2011a, PhRvL, 106, 201101
Adriani, O., Barbarino, G. C., Bazilevskaya, G. A., et al. 2011b, Sci, 332, 69
Amano, T., Katou, T., Kitamura, N., et al. 2020, PhRvL, 124, 065101
Aschwanden, M. J., Caspi, A., Cohen, C. M. S., et al. 2017, ApJ, 836, 17
Bale, S. D., Goetz, K., Harvey, P. R., et al. 2016, SSRv, 204, 49
Bamba, A., Ohira, Y., Yamazaki, R., et al. 2018, ApJ, 854, 71
Berezhko, E. G., Ksenofontov, L. T., & Voelk, H. J. 2009, A&A, 505, 169
Bohdan, A., Pohl, M., Niemiec, J., et al. 2020, ApJ, 904, 12
Decker, R. B., Krimigis, S. M., Roelof, E. C., et al. 2008, Natur, 454, 67
Drury, L. O. 1983, RPPh, 46, 973
Ellison, D. C., Giacalone, J., Burgess, D., & Schwartz, S. J. 1993, JGR, 98, 21085
Ellison, D. C., & Moebius, E. 1987, ApJ, 318, 474
Ellison, D. C., Moebius, E., & Paschmann, G. 1990, ApJ, 352, 376
Emslie, A. G., Dennis, B. R., Shih, A. Y., et al. 2012, ApJ, 759, 71
Fraschetti, F. 2013, ApJ, 770, 84
Fraschetti, F. 2021, ApJ, 909, 42
Fraschetti, F., & Giacalone, J. 2015, MNRAS, 448, 3555
Fraschetti, F., & Giacalone, J. 2020, MNRAS, 499, 2087
Giacalone, J. 2005a, ApJ, 624, 765
Giacalone, J. 2005b, ApJL, 628, L37
Giacalone, J. 2005, ApJ, 628, L37
Giacalone, J., Burgess, D., Schwartz, S. J., Ellison, D. C., & Bennett, L. 1997, JGR, 102, 19789
Giacalone, J., & Jokipii, J. R. 2007, ApJL, 663, L41
Giacalone, J., Burgess, D., Bale, S. D., et al. 2021, ApJ, 921, 102
Gloeckler, G., Balsiger, H., Bürgi, A., et al. 1995, SSRv, 71, 79
Gloeckler, G., Cain, J., Ipavich, F. M., et al. 1998, SSRv, 86, 497
Gold, R. E., Krimigis, S. M., Hawkins, S. E. I., et al. 1998, SSRv, 86, 541
Gosling, J. T., Asbridge, J. R., Bame, S. J., et al. 1981, JGR, 86, 547
Hanson, E. L. M., Agapitov, O. V., Mozer, F. S., et al. 2020, JGRA, 125, e27231
Hovey, L., Hughes, J. P., & Eriksen, K. 2015, ApJ, 809, 119
Jokipii, J. R. 1982, ApJ, 255, 716
Jokipii, J. R. 1987, ApJ, 313, 842
Jokipii, J. R., & Giacalone, J. 2007, ApJ, 660, 336
Kajdič, P., Hietala, H., & Blanco-Cano, X. 2017, ApJL, 849, L27
Kasper, J. C., Abiad, R., Austin, G., et al. 2016, SSRv, 204, 131
Kato, T. N. 2015, ApJ, 802, 115
Katou, T., & Amano, T. 2019, ApJ, 874, 119
Kim, S., Ha, J.-H., Ryu, D., & Kang, H. 2021, ApJ, 913, 35
Koval, A., & Szabo, A. 2008, JGRA, 113, A10110
Lario, D., Berger, L., Decker, R. B., et al. 2019, AJ, 158, 12
Lario, D., & Decker, R. B. 2002, GeoRL, 29, 1393
Lario, D., Decker, R. B., Roelof, E. C., & Viñas, A. F. 2015, ApJ, 813, 85
Lario, D., Ho, G. C., Decker, R. B., et al. 2003, in AIP Conf. Ser. 679, Solar Wind Ten, ed. M. Velli et al. (Melville, NY: AIP), 640
Lario, D., Richardson, I. G., Palmerio, E., et al. 2021, ApJ, 920, 123
Lin, R. P., Anderson, K. A., Ashford, S., et al. 1995, SSRv, 71, 125
Marhavilas, P. K., & Sarris, E. T. 2011, ITPS, 39, 1516
McComas, D., Alexander, N., Angold, N., et al. 2016, SSRv, 204, 187
Mewaldt, R. A., Cohen, C. M. S., Giacalone, J., et al. 2008, in AIP Conf. Ser., 1039, ed. G. Li et al. (Melville, NY: AIP), 111
Meziane, K., Wilber, M., Mazelle, C., Parks, G. K., & Hamza, A. M. 2005, in AIP Conf. Ser., Vol. 781, The Physics of Collisionless Shocks: 4th Annual IGPP Int. Astrophysics Conf., ed. G. Li, G. P. Zank, & C. T. Russell (Melville, NY: AIP), 116
Mitchell, J. G., Nolfo, G. A. D., Hill, M. E., et al. 2021, ApJ, 919, 119
Morlino, G., Amato, E., & Blasi, P. 2009, MNRAS, 392, 240
Owen, C. J., Bruno, R., Livi, S., et al. 2020, A&A, 642, A16
Parker, E. N. 1965, P&SS, 13, 9
Pohl, M., Hoshino, M., & Niemiec, J. 2020, PrPNP, 111, 103751
Reames, D. V. 2012, ApJ, 757, 93
Richardson, J. D., Kasper, J. C., Wang, C., Belcher, J. W., & Lazarus, A. J. 2008, Natur, 454, 63
Rigby, A., Cruz, F., Albertazzi, B., et al. 2018, NatPh, 14, 475
Rodríguez-Pacheco, J., Wimmer-Schweingruber, R. F., Mason, G. M., et al. 2020, A&A, 642, A7
Russell, C. T., Mewaldt, R. A., Luhmann, J. G., et al. 2013, ApJ, 770, 38
Savoini, P., Lembege, B., & Stienlet, J. 2013, JGRA, 118, 1132
Scholer, M., Shinohara, I., & Matsukiyo, S. 2003, JGRA, 108, 1014
Slane, P., Lee, S.-H., Ellison, D. C., et al. 2014, ApJ, 783, 33
Szabo, A. 1994, JGR, 99, 14737
Treumann, R. A. 2009, A&ARv, 17, 409
van Marle, A. J., Casse, F., & Marcowith, A. 2018, MNRAS, 473, 3394
Vazza, F., Eckert, D., Brüggen, M., & Huber, B. 2015, MNRAS, 451, 2198
Wilson, L. B., Chen, L.-J., Wang, S., et al. 2020, ApJ, 893, 22
Yuan, Q., Liu, S., & Bi, X. 2012, ApJ, 761, 133
Zank, G. P., Hunana, P., Mostafavi, P., et al. 2015, ApJ, 814, 137